Ferroelectric Bent Band Structure Studied by Angle-resolved Hard X-ray Photoemission Spectroscopy

Norihiro Oshime

September 7, 2018

Abstract

This thesis reviews that electronic structure of ferroelectrics shows a characteristic energy states affected by spontaneous polarization, which is a modern crucial issue in the ferroelectric research. Since discovery of ferroelectricity exhibited in the crystal structure of perovskite oxide, ferroelectric materials could have a huge contribution for industrial field for several decades. This activity also has stimulated scientific field. Thanks to the improvement of dielectric and piezoelectric performances, the industrial technique for multi-layered ceramic condensers and piezoelectric actuators has been developed using ferroelectric perovskites such as barium titanate and lead zirconate titanate, which become essential electronic devices. From the scientific view, ferroelectric materials historically have been treated as typical ionic crystal. Recently, this fact was changed by the consideration of polarization formation mechanism based on covalent nature in transition metal-oxygen hybridization. Modern ferroelectric science is thus focusing on the study of electronic structure.

The electronic structure of ferroelectrics has been predicted to have unique electronic energy states, that the energy levels of atomic orbitals show energy shift along the polarization direction from the surface to opposite side in the crystal. This phenomenon is called as band bending structure and has been attracted much attention in recent years. The band bending structure is a key property of recent developed functional devices such as nonvolatile random access memory and photovoltaic devices; however nobody can theoretically and experimentally elucidate this phenomenon.

X-ray photoemission spectroscopy is one of possible experimental techniques. Although it can measure the energy levels of atomic orbitals, the band bending structure is

difficult to see directly as explained below. First problem is a spatial resolution limited by the relation of x-ray beam size and ferroelectric domain size with sub-micrometer. So monodomain sample is required. But single crystal usually has a complex domain structure. Second is how to observe the energy levels in depth profile. Conventional photoemission spectroscopy cannot perform the layer by layer observation in the crystal, and also is adequate for a sample with high carrier concentration to avoid extrinsic charging effect, indicating that ferroelectric crystal is not ideal sample. Therefore, we considered that hard x-ray photoemission spectroscopy equipped with angle-resolved system (AR-HAXPES) is the best solution for accurate measurement of band bending structure. AR-HAXPES system can detect a signal emitted from each depth region by a changing of photoemission detection angle. This accuracy is permitted by the installation of wide angle objective lens because this equipment does not require any mechanical adjustment, performing one-shot photoemission detection with various angle. Furthermore, the combination of above instrument and the usage of specialized thin film for the monodomain structure performs perfect experiment. Monodomain structure fabricated on the conductive single crystal substrate can be prepared by pulsed laser deposition, which supplies photoemission detection with free from charging effect. By this idea, we succeeded to observe the band bending phenomenon in ferroelectrics for the first time. Our result proves principle mechanism of future ferroelectric devices such as random access memory and photovoltaic cell, contributing widely to academic and industrial fields.

Contents

1 INTRODUCTION **6**

2 EXPERIMENTAL **11**

2.1 $BaTiO_3$ treated as nanoparticles and thin films 11

2.1.1 Nanoparticles 11

2.1.2 Thin films 15

2.2 Reflectance spectroscopy and photoelectron yield spectroscopy 20

2.3 Angle-resolved hard x-ray photoemission spectroscopy 22

3 RESULTS AND DISCUSSION **25**

3.1 Band Structures controlled by ionic deficiency 25

3.2 Bent band structure induced by electric polarization 33

4 SUMMARY **43**

List of Figures

2.1 XRD patterns. All samples retain ABO_3 perovskite structure. In sample S, since BTO particles were fabricated by a hydrothermal synthesis method, they contained a small amount of $BaCO_3$ (less than 1 at%). In sample O, a Ba_2TiO_4 phase (less than 1 at%) appears during the post annealing. . . 13

2.2 SEM images. (a), (b), and (c) are samples S, O, and B, respectively. The surface morphology, shape and particles size of sample B are unchanged from sample S. In the case of sample O, grain growth has occurred because of post annealing. 14

2.3 (a) X-ray diffraction patterns of BTO and ALO films with 5 nm thickness on NSTO substrates. (b) Rocking curves measured at BTO *002* (blue dashed line) and ALO *004* (black line) diffractions. 18

2.4 (a) Topographic image of the BTO film. Piezoresponse phase images of BTO film: (b) +3 V ($2 \times 2\,\mu m^2$ area, outside) and −3 V ($1 \times 1\,\mu m^2$ area, inside) and (c) −3 V ($2 \times 2\,\mu m^2$ area, outside) and +3 V ($1 \times 1\,\mu m^2$ area, inside) writing treatments, with a measured area of $3 \times 3\,\mu m^2$. Light and dark regions correspond to negative and positive polarization directions, respectively. 19

2.5 Schematic picture of AR-HAXPES with wide-angle objective lens for BTO (or ALO) thin film. The angle between the AR-HAXPES apparatus and incident beam is fixed at 90° in all experiments. The lens has a 64° acceptance angle. Take-off angle (TOA) is defined as the angle between the sample surface and the lens. The emission angle of photoelectrons increases with increasing escape depth, their TOA was determined to be 35°. The inset shows AR-HAXPES spectra of O-1s in ALO. The probing depth in photoemission increases as the emission angle increases. Red and purple circles are surface and deeper regions, respectively. In the spectrum at emission angle = 65°, curves of background and Voigt function are drawn as gray lines. 23

3.1 UV-visible reflectance spectra of BTOs. Lines approximating the sudden decrease in reflectivity show the optical band gap E_{g}. 27

3.2 PYS spectra of BTOs. Lines approximate the photoemission energy IE. The inset shows the occupancy levels of valence electrons, as analyzed from the derivative of the photoelectron yield spectrum with respect to photon energy. Spectra A and B correspond to nearly pure O orbitals and hybridized states between O-2p and Ti-3d, respectively. 28

3.3 Energy diagrams of the valence and the conduction bands of BTOs. The energy diagrams include the values of E_g and I_E obtained from our two experimental techniques. Oxygen vacancies form the donor level below the conduction band and the acceptor level above the valence band, respectively. The shape of the valence band is determined by the derivative of the photoelectron yield spectrum. Regions A and B correspond to those in Fig. 3.2. 29

3.4 Angle-integrated HAXPES spectra of the 5 nm thick BTO. 37

3.5 AR-HAXPES spectra of Ti-$2p_{3/2}$ in the 5 nm thick BTO observed at various depths. Red and purple circles are surface and deeper regions, respectively. In the spectrum at emission angle = 65°, curves of background and Voigt function are drawn as gray lines. 38

3.6 AR-HAXPES spectra of valence band in 5 nm thick BTO observed at various depths. Red and purple circles are surface and deeper regions, respectively. In the spectrum at emission angle = 65°, curves of background and Voigt function are drawn as gray lines. 39

3.7 Depth dependence of binding energies of BTO: (a) Ti-$2p_{3/2}$, O-1s, Ba-$3d_{5/2}$ in 5 nm thickness and (b) Ti-$2p_{3/2}$ in 15 nm. Dots indicate the peak energy estimated by the center position of FWHM at each emission angle. Solid and dashed red lines are fitted by a linear function. Green arrows show the energy shift in FEBB. Red arrows indicate the direction of electric polarization. 40

3.8 Depth dependence of binding energies of valence band in the 5 nm thick BTO. Dots indicate the peak energy estimated by the center position of FWHM at each emission angle. Solid and dashed red lines are fitted by a linear function. Green arrows show the energy shift in FEBB. Red arrows indicate the direction of electric polarization. 41

3.9 Depth dependence of binding energies of Ti-$2p_{3/2}$ in 50 nm thick BTO. Dots indicate the peak energy estimated by the center position of FWHM at each emission angle. Solid and dashed red lines are fitted by a linear function. Green arrows show the energy shift in FEBB. Red arrows indicate the direction of electric polarization. 42

Chapter 1

INTRODUCTION

Applications of ferroelectrics are becoming steadily more numerous, as their high permittivity is used in multi-layered ceramic condensers (MLCC), their piezoelectricity in actuators, and their pyroelectricity in thermal sensors. Other recent areas where ferroelectrics are used include ferroelectric random access memory (FeRAM), and solar cells [1–4] in which the presence of electric polarization plays the central role. In the latter devices, the polarization reversal drives the switching of the band skew, which can control the carrier flow accordingly [4–6]. This function may open a new area in the study of ferroelectricity. Also, the study of ferroelectrics' electric polarization is naturally evolving from the covalent nature of the electronic orbitals between transition metals and oxide ions, spin lattice coupling in multiferroic materials, and the carrier transport involved in electric polarization [7–9].

In order to demonstrate new function derived from ferroelectricity, let us consider the electronic structure of ferroelectric in the heterostructure composed by metal, ferroelectric, and semiconductor. A spontaneous electric polarization of ferroelectric materials originates in the relative ionic displacement of a transition metal and oxygen, with inversion symmetry breaking. The electric field generated by the electric polarization causes an electrostatic potential gradient along the polarization direction in ferroelectric materials [10, 11], forming a bent band structure. Such a graduated potential influence on the energy levels of atomic orbitals drives rectification of electron transfer in the heterostructures such as ferroelectric tunneling junctions (FTJs) [5, 12–16] and photovoltaic (PV)

devices [2–4, 17]. FTJs, which is one of candidate structures of FeRAM, constructed of a ferroelectric thin film sandwiched by two different metals, i.e. metal (M)-ferroelectric (FE)-M junctions, exhibit electron tunneling across the barrier with an electrostatic potential gradient [13]. Switching polarization can drive the reversal of the gradient orientation producing a large tunneling electroresistance (TER) effect at M-FE-M junctions [14]. Recently, a TER effect with a magnitude of 10^4 has been demonstrated in M-FE-heavily doped semiconductor (hS) junctions, where the hS was Nb-doped $SrTiO_3$ (NSTO) [15,16]. At the FE-hS interface, the combination of a wide Schottky barrier width and the small work function of the NSTO create variable depletion and accumulation states controlled by polarization reorientation [5, 15, 16]. Since band engineering of the FE-hS interface can improve the effective electron transfer, FTJs are currently seen as a promising heterostructure for FeRAM, one of the several advanced ferroelectric functional devices. In contrast, in ferroelectric PV devices for solar cells with a slightly wide forbidden band (2-4 eV), the surface band bending induced by accumulating charges play an important role in photoconductivity [2–4, 17]. When photons in the ultraviolet energy range excite electronic carriers from valence to conduction bands, the electronic carriers can transfer to the crystal's surface along the electric polarization orientation, producing selective electron accumulation at the positive polarization surface [3, 4]. In photochemical reactions, ferroelectric substrates offer a significant advantage in the fabrication of nanostructures such as nano metals and organic molecules, because nanometer-sized polarization domains can be patterned in positive or negative regions by an external electric field [3, 4].

Electronic structures modulated by electric polarization yield a so-called ferroelectric band bending structure. Although band bending structures can be described by the effect of electric polarization on ferroelectric materials, the common band bending phenomenon

has been discussed as an interfacial effect in a pn junction, which consists of electrically non-polar semiconductors such as Si and GaAs [18]. Since the band bending structure in a pn junction is derived from the different work functions of two semiconductors, it cannot be reversed by any external field. In contrast, the ferroelectric band bending structure is made possible by reversible electrical polarization. The bent-band structure of pn junctions has been observed by transmission electron microscopy [19]; however, the actual basis of ferroelectric band bending remains obscure.

One of the crucial problems is that the actual location of the band structure of ferroelectrics is not known. Because ferroelectrics have been considered to be typical insulators. As seen in a large number of studies on the M-FE-M and M-FE-hS junctions mentioned above, controlling the levels of the conduction and valence bands in ferroelectrics still remains a challenge. While some reports suggest that the band structure in ferroelectrics has been confirmed by first-principles calculations [20, 21] and photoelectron spectroscopy of doped single crystals [22,23], the absolute value of the energy levels remains unclear. Thus, we consider that a quantitative understanding of ferroelectric semiconductor properties, and especially the accurate determination of the depth of the electronic energy bands, remains important before elucidation of band bending structure. It is expected that typical ferroelectric insulators become semiconductors upon doping, which form donor or acceptor levels below the conduction band or above the valence band, respectively [24]. While the band structure of ferroelectric oxides is characterized as a wide band gap [6], ferroelectric compounds produced by ordinary preparation methods include sites where an expected ion is absent: ionic vacancies. $BaTiO_3$ (BTO) with oxygen vacancies forms donor levels under the conduction band and becomes an n-type semiconductor, just as in the case of donor ion doping [25]. Moreover, BTO when heavily reduced by annealing

in H_2 becomes an n-type semiconductor or even a metal, but retains ferroelectricity [26]. On the other hand, BTO with cation vacancies is expected to be a p-type semiconductor and to form an acceptor level above the valence band [27]. As BTO is classified as a typical ferroelectric oxide semiconductor, we may control its semiconductor properties, such as the donor/acceptor levels formed by ionic defects and substitution [28]. However, it remains unclear how the impurity level, valence band, and conduction band are related to ionic vacancies in a ferroelectric even though that we do not have any information of bent band structure.

The purpose of the present study is to elucidate the band bending structure of ferroelectrics. Here we propose a strategy for the present study. First, we attempt to visualize and quantify the band structure of ferroelectric BTO particles by observing its changes when modified by alterations of the ionic vacancy structure. The band gap is estimated by optical reflectance spectroscopy and the ionization energy is then estimated by photoelectron yield spectroscopy (PYS), which allows us to quantify the band structure. However, above method cannot lead the elucidation of the bent-band structure. It is attributed to the restriction of special resolution of measurement system. We consider that knowing the energy shift of atomic orbitals in terms of their depth profile is an important basis for understanding the electronic structure in ferroelectrics. As second mission, we perform the angle-resolved hard x-ray photoemission spectroscopy (AR-HAXPES) experiment on the ferroelectric BTO thin films, emphasizing the direct observation of the band bending structure in ferroelectric materials.

In the next chapter, we will explain the details of ferroelectric BTO particles and thin films as a sample preparation, and optical reflectance spectroscopy, PYS and AR-HAXPES as a measurement technique. In the chapter 3, we will refer to the result

observed by these methods mentioned in the chapter 2. Particularly, the present system of AR-HAXPES is confirmed to be excellent to detect the depth profiles of both core and valence orbitals. These results are discussed in the same section. The results and discussions reveal the existence of ferroelectric band bending structure and elucidate principle mechanism for future ferroelectric devices such as FeRAM and solar cells. Our finding may encourage ferroelectric research in both academic and industrial fields.

Chapter 2

EXPERIMENTAL

2.1 $BaTiO_3$ treated as nanoparticles and thin films

2.1.1 Nanoparticles

Three types of BTO, oxygen and / or barium deficient, and relative stoichiometric BTO particles were used in the present study, which we abbreviate to as samples O, B and S, respectively. Commercial BTO nanopowder (sample S) was used to form samples O and B. This was stoichiometric BTO powder purchased from Kanto Denka Kogyo Co., Ltd. It was formed by hydrothermal synthesis, with a Ba / Ti ratio of 1.0(3) and an average particle size of 50 nm as determined by inductively coupled plasma atomic emission spectroscopy (ICP-AES) and dynamic light scattering particle size analysis, respectively. BTO samples with anion and cation vacancies (samples O and B, respectively) were prepared by annealing in a reducing atmosphere, and washing in concentrated nitric acid, respectively. To perform the oxygen reduction and obtain sample O, the stoichiometric BTO was annealed in a muffle furnace at 1150°C with a flowing mixture of 5% H_2 and 95% Ar for 64 h. To prepare sample B, with cation vacancies, the sample S was dispersed in concentrated nitric acid (0.75 mol/L), then agitated, decanted at room temperature and dried in a furnace at 110°C in ambient atmosphere.

Powder x-ray diffraction (XRD) patterns show that both of the ion-deficient samples (samples O and B) retain an ABO_3 perovskite structure as shown in Fig. 2.1. The purity of the single phase was confirmed in both samples by the XRD measurement, resulting

that with $BaCO_3$ and Ba_2TiO_4 phases are included less than 1 at% in samples S and O, respectively. A small amount of $BaCO_3$ was included (less than 1 at%) since BTO particles were fabricated by a hydrothermal synthesis method. Such a small amount cannot have affected our experimental result. A Ba_2TiO_4 phase appeared in sample O as a result of post annealing (1150°C, 64 h). This tendency is similar to the result reported in Ref. [29]. Since contamination is less than 1 at%, this cannot be affected to our experiment.The presence of cation vacancies in sample B was less than several at% because the lattice parameter of the a-axis barely changed from 4.007 Å (sample S) to 4.005 Å (sample B). The lattice parameters were determined by Rietveld analysis using RIETAN-FP [30]. ICP-AES also showed that the Ba / Ti ratio of $BaTiO_3$ has been reduced from 1.0(4) to 0.96(7) by nitric acid treatment. Figure 2.2 shows scanning electron microscope (SEM) imagery of samples. The surface morphology, shape and particles size of sample B are unchanged from sample S. The barium vacancy distribution in sample B is expected to be inhomogeneous, i.e. the value in the vicinity of the particle surface is much higher than that inside the particles. It is difficult to evaluate the distribution of cation vacancies in this case, but we think that inhomogeneity of barium vacancies has only negligible effects on our research. The reasons why are that: (1) Sample B consisted solely of 50 nm particles. If inhomogeneous vacancies were distributed within the interior of such small particles, that factor may be negligible. Since nitric acid can migrate into $BaTiO_3$ nano particles, we consider that any inhomogeneity caused by this process is negligible for our current purposes. (2) PYS and optical reflectance spectroscopic measurements are surface sensitive.

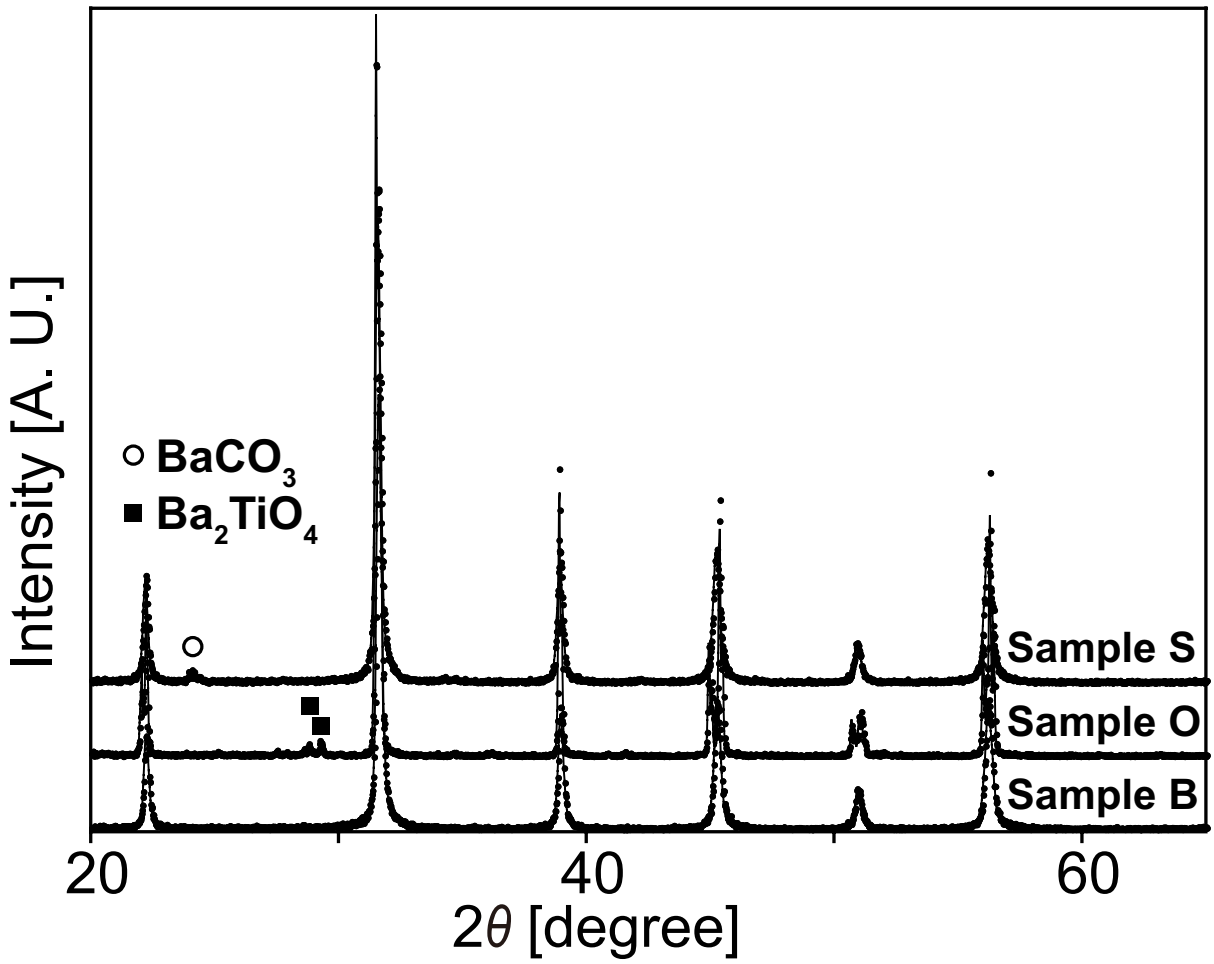

Figure 2.1: XRD patterns. All samples retain ABO_3 perovskite structure. In sample S, since BTO particles were fabricated by a hydrothermal synthesis method, they contained a small amount of $BaCO_3$ (less than 1 at%). In sample O, a Ba_2TiO_4 phase (less than 1 at%) appears during the post annealing.

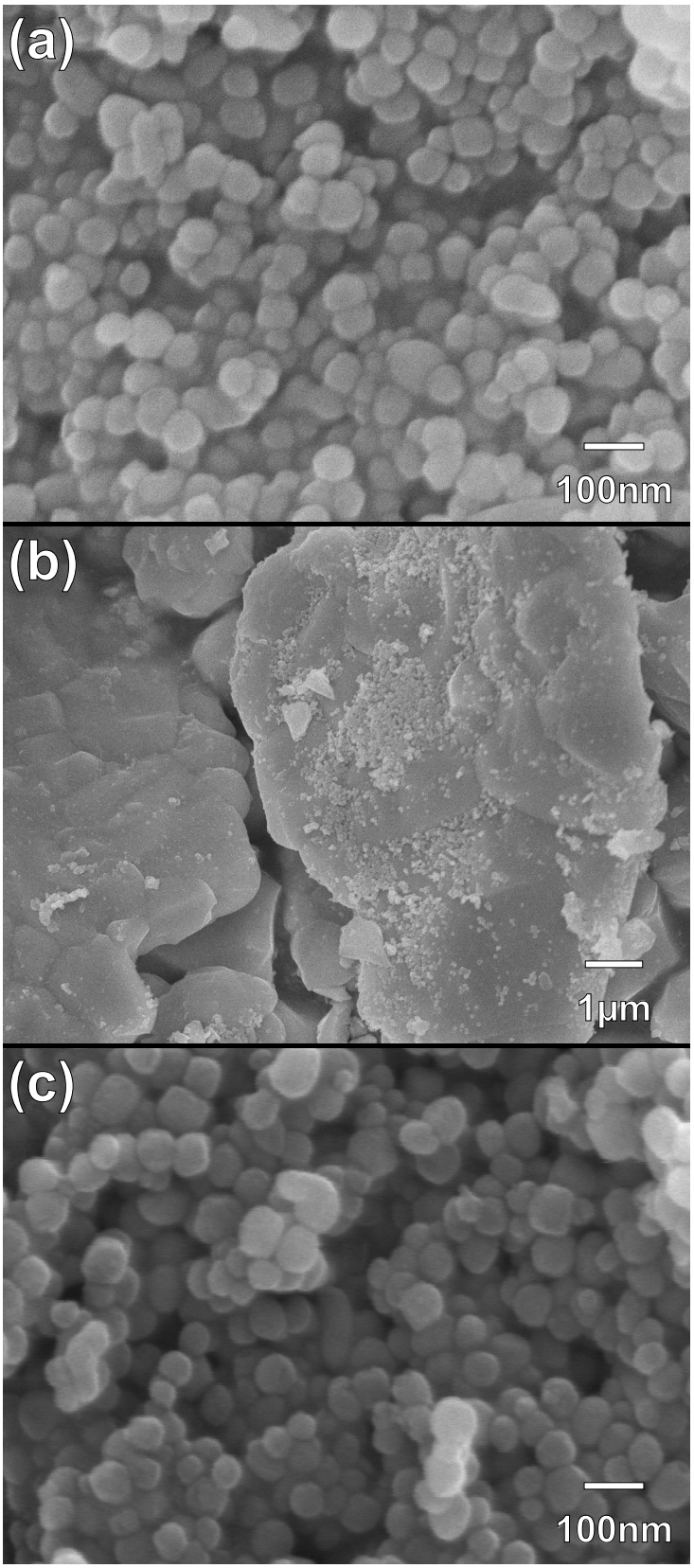

Figure 2.2: SEM images. (a), (b), and (c) are samples S, O, and B, respectively. The surface morphology, shape and particles size of sample B are unchanged from sample S. In the case of sample O, grain growth has occurred because of post annealing.

We considered the possibility of titanium vacancies in sample B, but ICP-AES analysis confirmed that titanium vacancies were not present. This result implies that the barium vacancies are significantly induced but titanium vacancies are not.

2.1.2 Thin films

For AR-HAXPES measurement, epitaxial ferroelectric oxide thin films grown on conductive substrates were used. Because conventional ferroelectric oxides have small carrier concentrations, resulting in charge at the surface and making effective photoemission detection difficult. The conductive substrate also works as a bottom electrode for the polarization switching. We prepared two types of samples. One is for observation of the thickness dependence. Ferroelectric BTO thin films with 5 and 15 nm thickness were deposited on (100) NSTO (Nb 0.5wt% doped) single-crystal substrates by pulsed laser deposition, using the 266 nm 4th-harmonic wave of a Nd:YAG laser. Non-ferroelectric γ-Al_2O_3 (ALO) was also prepared to confirm depth profile in the heterostructure. Second is for observation of the polarization switching dependence. Pt/BTO/$SrRuO_3$ (SRO) was deposited on (100) ($LaAlO_3$)-($SrAl_{0.5}Ta_{0.5}O_3$) (LSAT) single crystal by the same way, where the thickness of Pt, BTO and SRO are 3, 50 and 50 nm, respectively. Deposition conditions of BTO and ALO were respectively 650°C and 700°C growth temperature, 20 mTorr and 1 mTorr oxygen pressure, and 1.3 and 2.9 J/cm^2 of laser energy. Our experiment aimed to investigate the contribution of polarization to band bending. In this case, simple interface using single domain BTO thin film with avoiding any ferroelectric and ferroelastic domain contributions is necessary to understanding. Crystal structures of the deposited films were confirmed by high-resolution x-ray diffraction (XRD, Smartlab RIGAKU) with a 2-bounce monochromator. The polarization direction of the BTO film was measured by piezore-

sponse force microscopy (PFM, MFP-3D Oxford instruments). Figure 2.3(a) shows XRD θ–2θ patterns of BTO and ALO films with 5 nm thickness. Both films were epitaxially grown with a cube-on-cube relation between film and substrate; (001)BTO ∥ (001)NSTO and (100)BTO ∥ (100)NSTO, (001)ALO ∥ (001)NSTO and (100)ALO ∥ (100)NSTO, respectively. Rocking curves of both films measured at *002* BTO and *004* ALO are shown in Fig. 2.3(b) and full-width at half-maximum (FWHM) values were 0.137° (blue dashed line) and 0.108° (black line). There were no secondary and no different orientation peaks in both films. The crystal mosaicities of both films were almost identical, as indicated by similar FWHM values.

Figure 2.4(a) shows a topographic image of 5 nm BTO thin film measured together with PFM. BTO film has the very flat surface with a root-mean-square roughness of 0.2 nm. As shown in Fig. 2.4(b), positive 3 V writing on a $2 \times 2\,\mu\mathrm{m}^2$ area was performed for poling treatment along substrate surface normal, then negative 3 V writing under $1 \times 1\,\mu\mathrm{m}^2$ at the center of a $2 \times 2\,\mu\mathrm{m}^2$ area was also performed. Additionally, the opposite bias for the same writing configuration was applied to the same BTO film, as shown in Fig. 2.4(c). Both the as-deposited area and the negative-bias writing area showed the same PFM phase contrast, although contrariwise, a positive bias writing area showed the opposite PFM phase contrast. No in-plane contribution of ferroelectricity was found by PFM measurement because this BTO film with the very thinner thickness was grown on NSTO substrate with the fully compressive strain from STO. The reason is that a lattice parameter of STO substrate is smaller than that of BTO. In the case of BTO, it is well known experimentally and theoretically that tetragonality is enhanced by compressive strain [31]. Therefore, BTO film with 5 nm thickness has only single *c*-domain and their polarization direction is headed to the substrate (down). The thickness of 15 nm has the

same direction. But 50 nm BTO deposited on SRO/LSAT has opposite direction (up) owing to the difference of substrate [32]. Note that, ALO thin film did not show any piezoresponse.

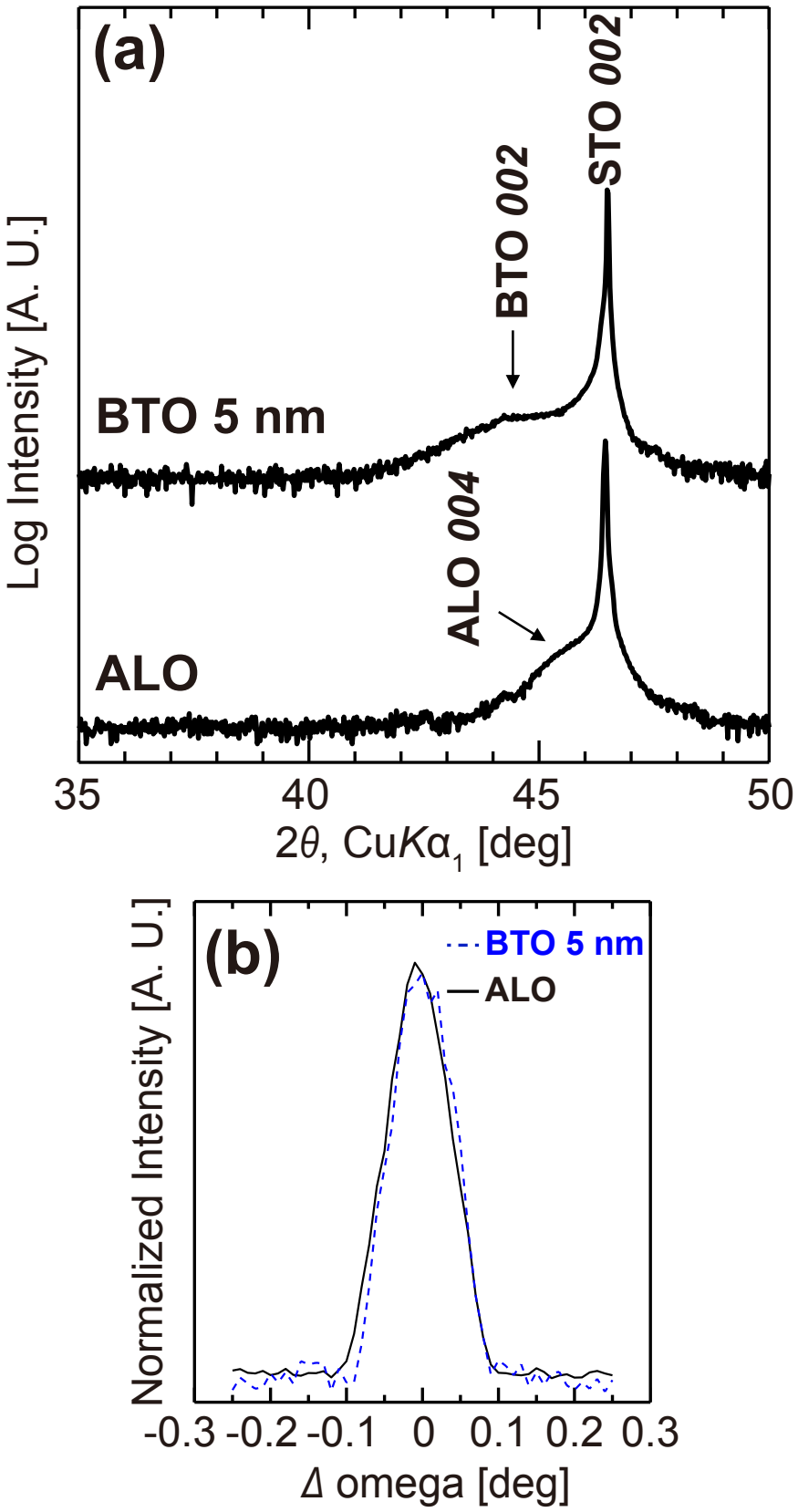

Figure 2.3: (a) X-ray diffraction patterns of BTO and ALO films with 5 nm thickness on NSTO substrates. (b) Rocking curves measured at BTO *002* (blue dashed line) and ALO *004* (black line) diffractions.

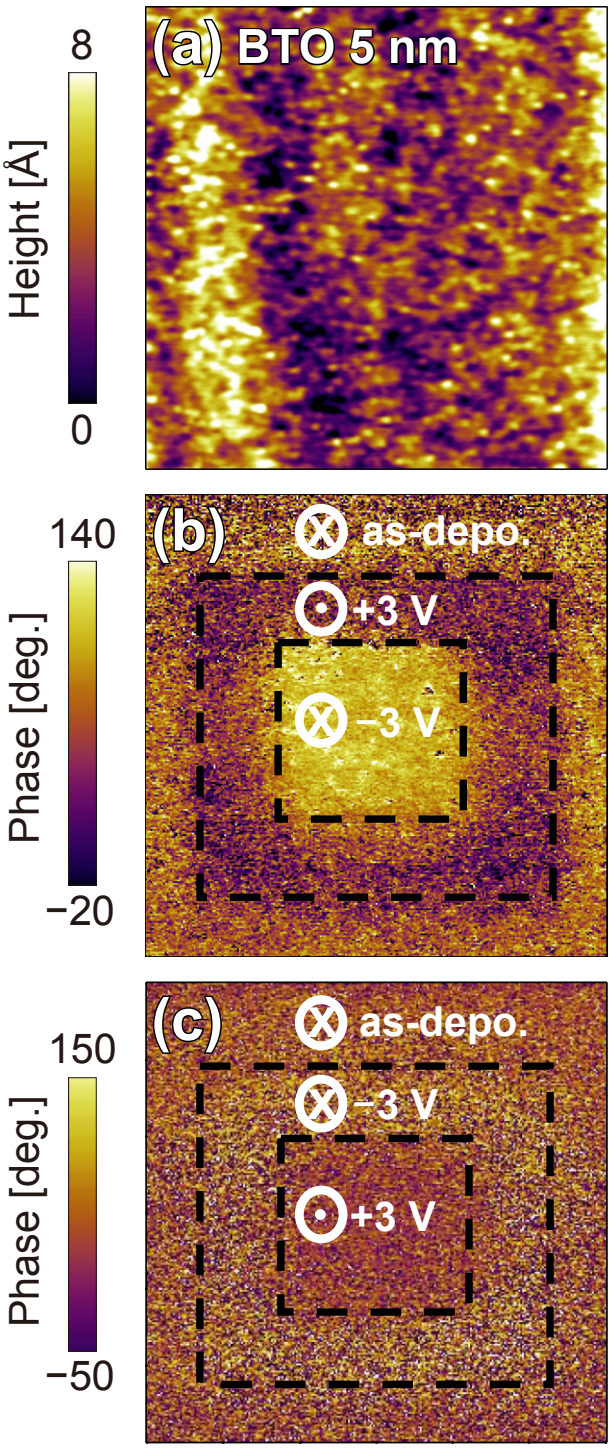

Figure 2.4: (a) Topographic image of the BTO film. Piezoresponse phase images of BTO film: (b) +3 V ($2 \times 2\,\mu m^2$ area, outside) and −3 V ($1 \times 1\,\mu m^2$ area, inside) and (c) −3 V ($2 \times 2\,\mu m^2$ area, outside) and +3 V ($1 \times 1\,\mu m^2$ area, inside) writing treatments, with a measured area of $3 \times 3\,\mu m^2$. Light and dark regions correspond to negative and positive polarization directions, respectively.

2.2 Reflectance spectroscopy and photoelectron yield spectroscopy

We consider that the levels of the valence band maximum (VBM) and the conduction band minimum (CBM) relative to vacuum level (E_{v}) are determined by the combination of the ionization energy (I_E) and optical band gap (E_{g}).

The E_{g} was measured with UV and visible light reflectance spectroscopy, using a UV and visible light spectrometer (JASCO Corp., V-550) with an integrating sphere attachment. The powder sample was pressed onto the fused silica glass and set in the corner of an integrating sphere placed in the spectrometer. The irradiation wavelength range was swept by two types of light source with a monochromator. The beam was diffused by the sample surface, then collected by the integrating sphere as reflectance spectrum. The E_{g} value was determined from the intersection point between the extrapolation lines of the high energy side and the drop-off side of the reflectance spectrum.

The I_E, which corresponds to the level of the VBM relative to E_{v}, was measured with PYS. This measurement was carried out using an ionization energy measurement system (Bunkoukeiki Co., Ltd, BIP-KV201). PYS measurement involves the observation of the external photoelectric effect [33]. The photocurrent (corresponding to photoelectron yield) emitted from the sample surface by a sweeping incident UV light beam was measured electrically. Generally, a technique like UV photoelectron spectroscopy (UPS) can measure the velocity of the photoelectrons using the open counter system [34]. It is well known that UPS is adequate for conductive samples, but that insulating samples are difficult to measure. However, a PYS system can detect the current of photoelectrons by applying a voltage bias to the sample, allowing the easy determination of I_E in highly insulating

oxides. In the present study, a $-30\,\mathrm{V}$ bias was applied to the highly insulating BTO samples . A detailed description of the PYS system can be seen in Fig. 1(a) in Ref. [33]. There are a few points of difference between our experimental setup and this figure. We measured powder samples connected to the bottom electrode with conductive carbon tape in an N_2 atmosphere at 60 Pa. Photoelectrons were emitted from the sample surface under UV irradiation, and then trapped by a ring-shaped electrode. Thus, accurate I_E measurement was achieved without interference from space charges. Generally, a photoelectron yield spectrum Y is expressed in terms of I_E as follows:

$$Y \sim (h\nu - I_E)^n \tag{2.1}$$

Here, $h\nu$ is the energy of the UV photons, and n can be any rational number from 1 to 3 [35,36]. In the present study, we used $n = 3$. We consider that the photoemission energy corresponds to the inflection point on the $Y^{1/3}$ spectrum. The I_E value was determined by the intersection point of two tangent lines at the inflection points (see Fig. 3.2). $\partial Y/\partial(h\nu)$ gives the variation of the occupied electronic states relative to energy [37]. Therefore, PYS can reveal the shape of the occupied electronic energy bands and their density of states (DOS) using the derivative of Y with respect to $h\nu$.

Penetration depth in PYS measurement is about 10 nm, which was confirmed by our other experiment using thin film. So we think that PYS measurement is surface sensitive. In the case of optical reflectance spectroscopy, penetration depth can be much deeper for the visible light range. However, this tendency cannot interfere with the determination of band gap energy, because the band edge lies in the ultra-violet range.

2.3 Angle-resolved hard x-ray photoemission spectroscopy

AR-HAXPES was carried out at BL47XU beamline in SPring-8. The detailed experimental setup of the BL47XU is described in Ref. [38]. Generally, the ionization cross-section decreases with increasing photon energy [39]. The required photon energy is estimated to be 8 keV when taking into account the escape depth of each atomic orbital. In the present study, a photon energy of 7.94 keV with a bandwidth of 38 meV was obtained using the Si (111) double monochromator and the Si (444) channel-cut monochromator. The x-ray beam was focused to 30×40 (samples without top electrode) or $1 \times 5\,\mu m^2$ (samples with Pt top electrode) regions on the sample surface. The AR-HAXPES apparatus installed in BL47XU has a wide-acceptance-angle objective lens ahead of the conventional HAXPES system (R-4000-VG-Scienta Co.) [38]. The angle between the AR-HAXPES apparatus and photon propagation is fixed at 90° in all experiments. The emission angle of photoelectrons depends on the escape depth as shown in Fig. 2.5. The objective lens has a wide acceptance angle of 64°. Since angular resolution corresponds to depth resolution from the sample, photoemission detection by the objective lens produces a wide depth-dependent analysis with a resolution of 1.32° even with a one-shot and fixed optical system. On the other hand, a conventional AR-HAXPES without a wide-angle objective lens is often required to mechanically adjust the optical angle between the incident beam and the sample, a feature causes difficulty in accurate angular-resolution and beam-positioning within the micrometer domain on samples. The energy resolution was estimated to be about 0.27 eV by Au Fermi-edge measurement.

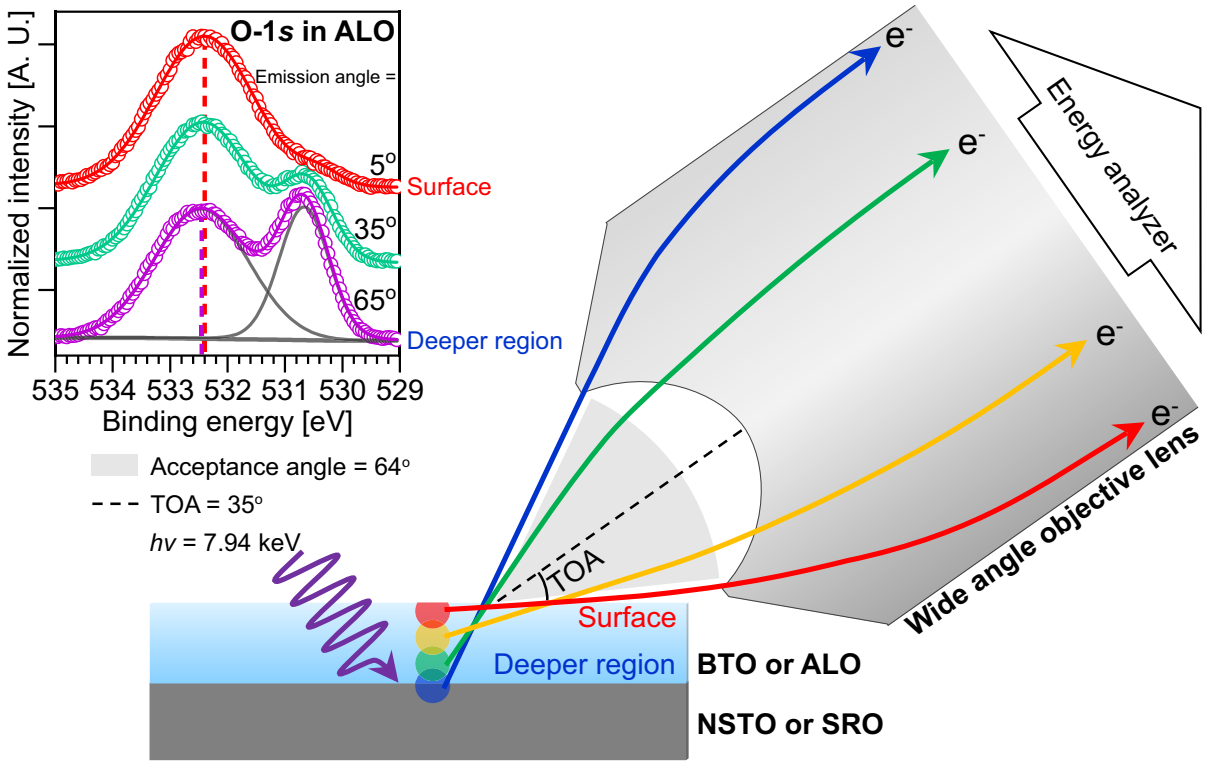

Figure 2.5: Schematic picture of AR-HAXPES with wide-angle objective lens for BTO (or ALO) thin film. The angle between the AR-HAXPES apparatus and incident beam is fixed at 90° in all experiments. The lens has a 64° acceptance angle. Take-off angle (TOA) is defined as the angle between the sample surface and the lens. The emission angle of photoelectrons increases with increasing escape depth, their TOA was determined to be 35°. The inset shows AR-HAXPES spectra of O-1*s* in ALO. The probing depth in photoemission increases as the emission angle increases. Red and purple circles are surface and deeper regions, respectively. In the spectrum at emission angle = 65°, curves of background and Voigt function are drawn as gray lines.

Polarization switching of 50 nm sample has been done using a function generator (WF1947, NF corp.) with the current-voltage ($I - V$) curves monitoring [40]. The function generator contacted to the bottom electrode (SRO) by silver wire with a 20 μm diameter, and a top electrode (Pt) was connected to the ground. A frequency range for an ac voltage was 500 kHz with an amplitude of 6 V_{pp} (peak-to-peak voltage). For polarization pointing down, 3 cycles ac voltage with a dc voltage of -2 V applied to the sample. -2 V nearly corresponds to a coercive field of 50 nm sample. Applied dc voltage was kept during AR-HAXPES measurement.

Chapter 3

RESULTS AND DISCUSSION

3.1 Band Structures controlled by ionic deficiency

Figure 3.1 shows the optical reflectance spectra. The signal intensity decreases sharply above E_g. Above 3 eV, the reflectance of sample S drops to its lowest value, due to an optical transition from the valence to the conduction band. Thus E_g for sample S was estimated to be 3.4 eV ($= E_g^S$). Sample B shows a similar E_g with the slightly wider value of 3.5 eV ($= E_g^{Ba}$). Sample O shows a smaller E_g estimated to be 3.3 eV ($= E_g^O$). The slight increase in reflectance for sample O above E_g^O comes from specular reflection, due to the grain growth of BTO particles during post annealing. The low optical reflectance of 30% even in the visible light region below E_g^O indicates the existence of an impurity energy level formed within the gap states, as will be described later.

Figure 3.2 shows the PYS spectra. The $Y^{1/3}$ plots gradually increase from the low energy region but clearly show the inflection point. Sample S shows its inflection point at 6.9 eV, indicating that photoelectron emission occurs above this energy level. The I_E of sample S is estimated to be 6.9 eV ($= I_E^S$).

The excessive photoelectron yield relative to the extrapolated line above 8 eV implies the existence of an additional band above 8 eV. It is noteworthy that numerous states in the valence band are formed from three electronic states [22, 41], one nearly pure O-2p orbital and two hybridization states originated from O-2p and Ti-3d orbitals. The inset in Fig. 3.2 shows the occupancy level of electrons located above the top of the valence

band, derived from the differentiation explained in the experimental section.

With references [22] and [41] for comparison, we concluded that the nearly pure O-2p orbital and one of the hybridized states correspond to regions A and B, respectively. The other hybridized states lie in higher energy level. The quantitative values of energy levels relative to E_{v} obtained from our experiments are in good agreement with the relative values of energy levels derived from x-ray photoelectron emission or UPS measurements and density functional theory calculations [22, 41]. The I_E of sample O is estimated to be 7.1 eV ($= I_E^{\mathrm{O}}$). The $Y^{1/3}$ in this case shows a similar tendency to that of sample S above 8 eV. As seen in the inset in Fig. 3.2, the DOS decreases with the introduction of oxygen vacancies.

The I_E of sample B is estimated to be 7.3 eV ($= I_E^{\mathrm{Ba}}$). The $Y^{1/3}$ plot shows a shift to a higher energy region compared with sample S. The DOS around the top of the valence band decreases with an increase in barium vacancies, which is similar to the case with oxygen vacancies.

As discussed above, the experimental results reflect the variations of VBM and CBM in each sample. Figure 3.3 shows the energy diagrams estimated from our experimental results. The CBM and VBM of sample S are at 3.5 eV and 6.9 eV, estimated from E_{v}. The valence band has a characteristic shape, which shows two electronic states, A and B, as noted in Fig. 3.2. Sample O shows a low density in region A, implying a decrease in O-2p states due to oxygen vacancy. From PYS spectra as in Fig. 3.2, sample B also has reduced density in region A, and also shows a shift of region B to lower energies. We consider that these changes originate in microscopic phenomena, which the formation of oxygen vacancies results in a decrease in O-2p states.

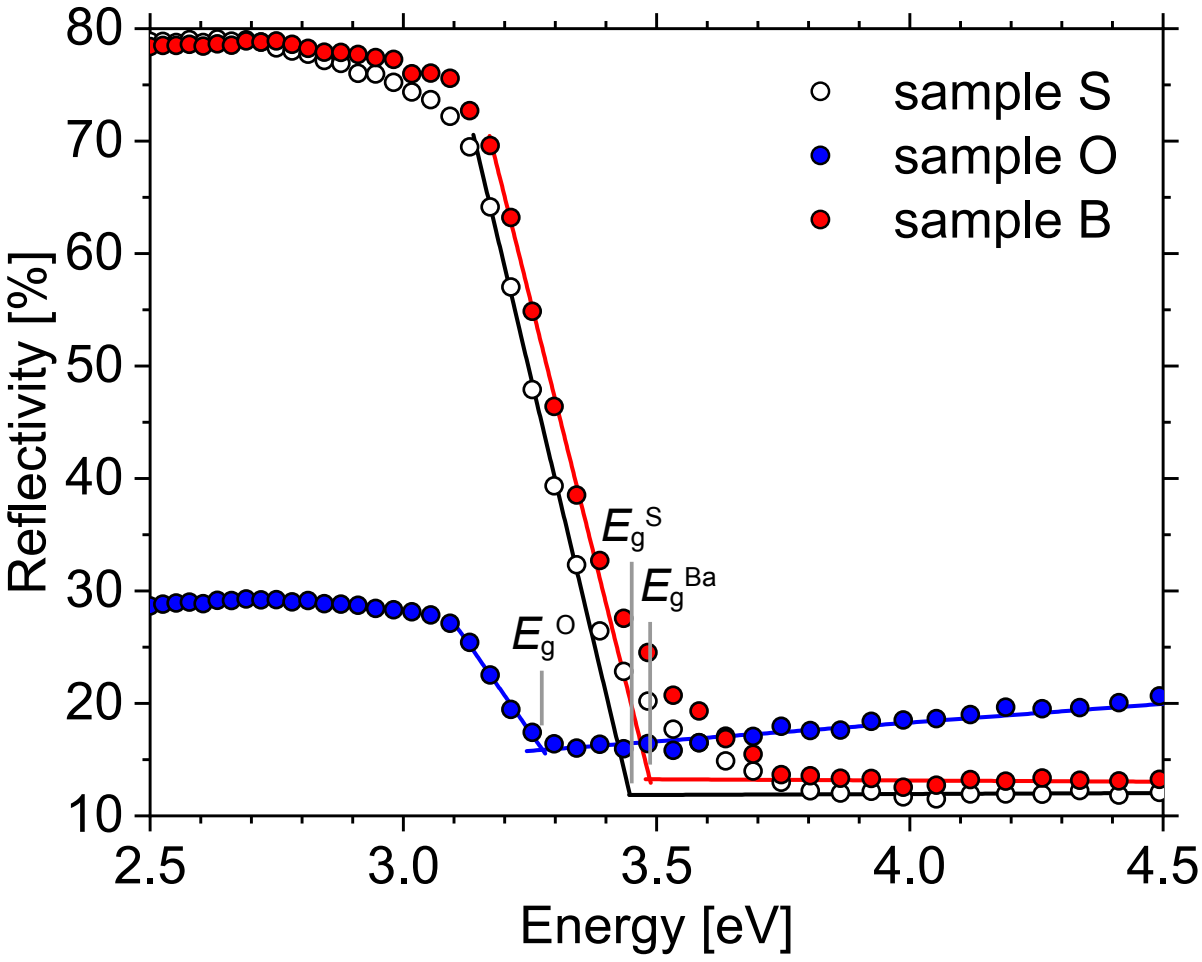

Figure 3.1: UV-visible reflectance spectra of BTOs. Lines approximating the sudden decrease in reflectivity show the optical band gap E_g.

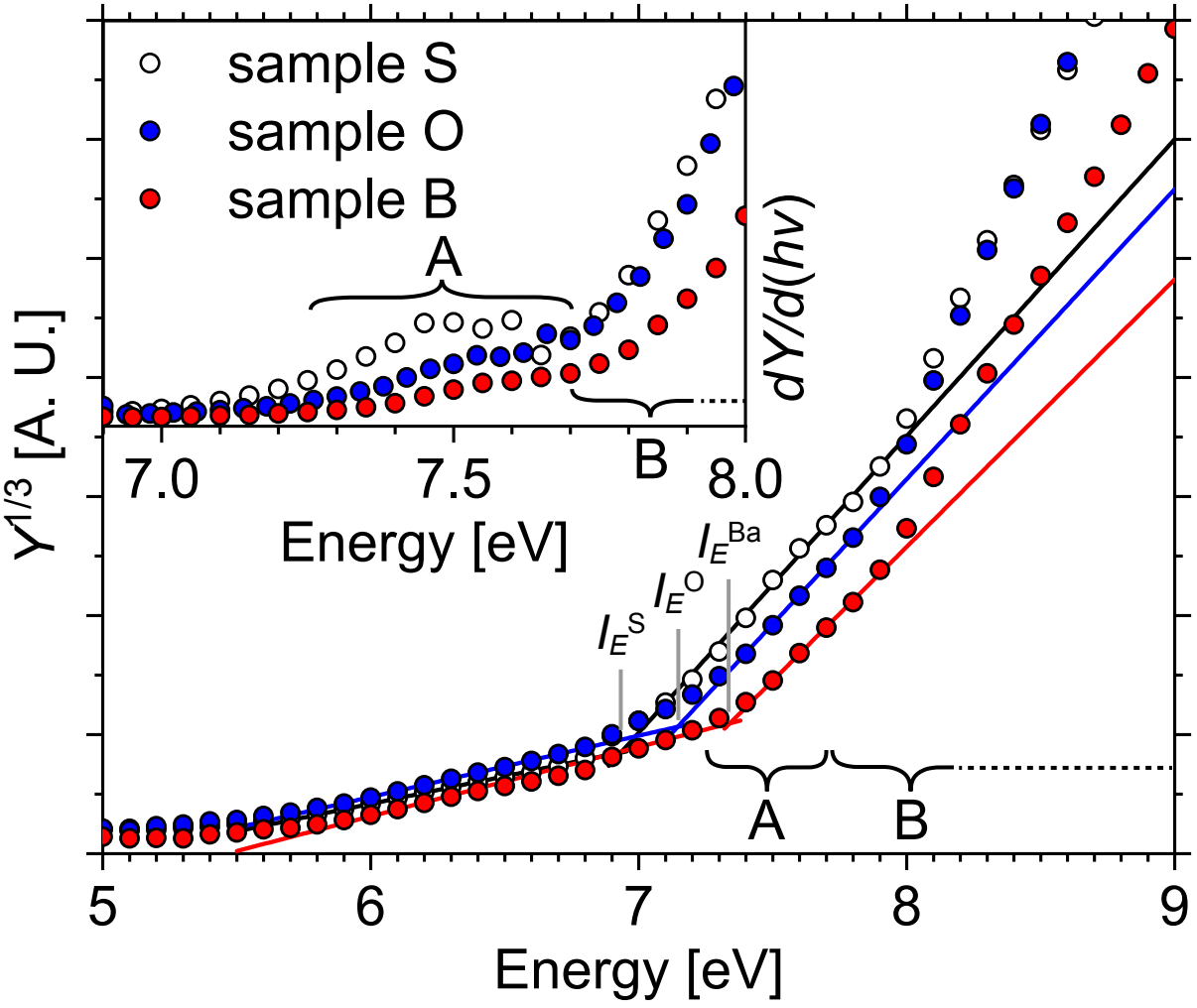

Figure 3.2: PYS spectra of BTOs. Lines approximate the photoemission energy IE. The inset shows the occupancy levels of valence electrons, as analyzed from the derivative of the photoelectron yield spectrum with respect to photon energy. Spectra A and B correspond to nearly pure O orbitals and hybridized states between O-2p and Ti-3d, respectively.

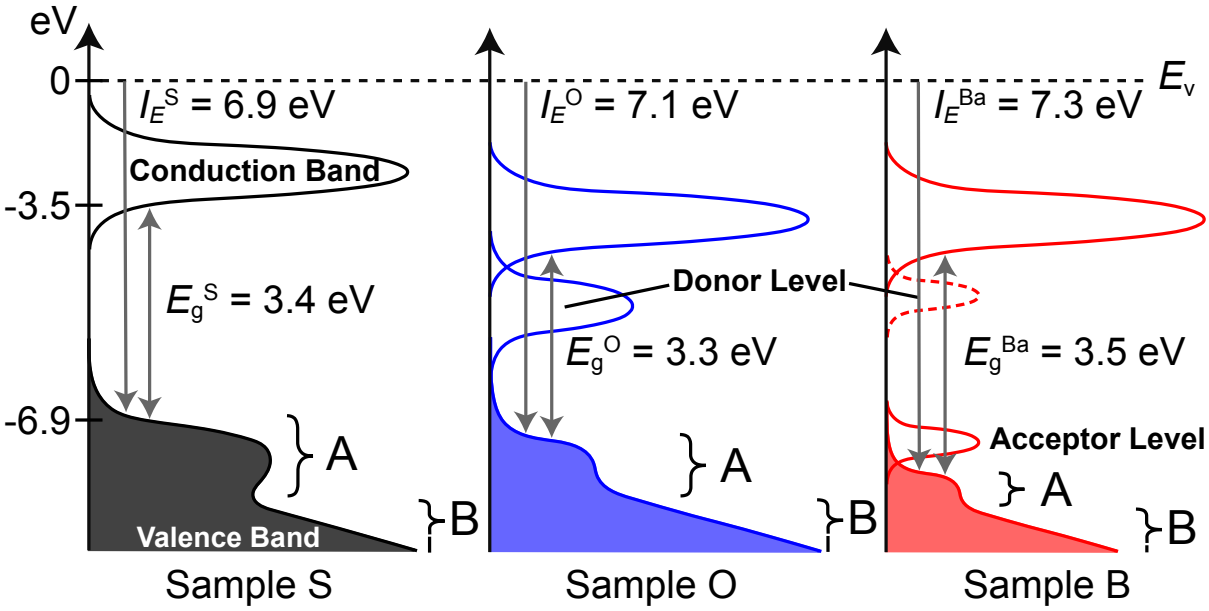

Figure 3.3: Energy diagrams of the valence and the conduction bands of BTOs. The energy diagrams include the values of E_g and I_E obtained from our two experimental techniques. Oxygen vacancies form the donor level below the conduction band and the acceptor level above the valence band, respectively. The shape of the valence band is determined by the derivative of the photoelectron yield spectrum. Regions A and B correspond to those in Fig. 3.2.

Generally, the semiconducting properties of covalent semiconductors such as III-IV elements are derived from ionic substitution [18]. In this case, the population of atomic orbitals does not change after ionic substitution. However, our samples can potentially change the population of atomic orbitals because ion-vacancy is the dominant factor rather than ion-substitution, indicating that effective mass of ions in samples B and O is lower than in sample S. It is reasonable that the oxygen vacancies can change the density of states near the VBM and CBM. As another possibility, our experimental result shows that an introduction of oxygen vacancies changes the energy distribution of occupancy states in the valence band by the formation of defect levels. First, some electrons in the valance band transfer into defect level. And then, valence band apparently shrinks accompanying that VBM shifts to lower level. This behavior is also shown in GaAs [37]. This interpretation is consistent with our PYS result seen in the inset of Fig. 3.2.

It is known that oxygen vacancies also induce the formation of a donor level. During optical reflectance spectroscopy, valence electrons can be excited from the valence band to the donor level [18]. As shown in Fig. 3.1, the low reflectivity of sample O indicates the formation of a broad donor level in the gap states. Since valence electrons are excited to the donor level by the energy of visible light, the donor level cannot be observed by PYS. On the other hand, no acceptor level has been observed by either reflectance spectroscopy or PYS. Although the anion and cation vacancies form donor and acceptor levels, respectively, the formation of an impurity level has a complicated mechanism.

We argue that an impurity level caused by cation vacancies is accompanied by charge compensation from anion vacancies. We confirmed that the observed behavior is similar to $Ba_{0.8}SrTi_{1-x}Mg_xO_3$ with substitution of Mg^{2+} for Ti^{4+} [42]. Since no decrease in optical reflectance in the visible light region was observed (Fig. 3.1) in the case of sample B, we

could not confirm the formation of a donor level in sample B. Therefore, we concluded that sample B had a small donor level compared to sample O. Though both donor and acceptor levels are formed in sample B, the acceptor level has not been experimentally observed in either the optical reflectance or the PYS measurements. This could be explained by the possibility that valence electrons excited from the valence band might be recoupled with holes on the acceptor level. To explain the high value of $E_{\mathrm{g}}^{\mathrm{Ba}}$ compared with other BTOs, we must consider the following. Holes are generated in the VBM by the acceptor level, resulting in the formation of unoccupied states in the VBM. At the same time, compensating oxygen vacancies lower the energy of the valence band. As a result, $E_{\mathrm{g}}^{\mathrm{Ba}}$ increases, relative to other BTOs. In PYS measurement, holes are compensated for by electron carriers injected from the bottom electrode due to the voltage bias. As a result, PYS measurement cannot detect an unoccupied level in the VBM.

Furthermore, the CBM is shifted to lower energies by induced oxygen vacancies. It is possible that titanium vacancies will cause the DOS of the Ti-3d states in the conduction band to decrease its shift toward the Ev. Because no titanium vacancies were confirmed in sample B, this effect is negligible. As another possibility for sample O, the Ti valence could be reduced from 4+ to 3+ to compensate for oxygen vacancies, though this was also not detected in this study. If Ti^{3+} states are formed in BTOs, Ti-3d states could be observed as optical absorption lines in the gap states. However, this spectral evidence was not confirmed for sample O in Fig. 3.1. Although the detailed mechanism remains unclear, we interpret that the conduction band has shifted to lower energies, and the valence band shifted due to the reduced density of O-2p orbitals [43].

Note that introduction of barium vacancies widens the band gap. Since barium vacancies can induce a small number of oxygen vacancies with accompanying charge compen-

sation, this behavior suppresses the excessive formation of donor levels in the gap states, indicating that cation vacancies can control the number of both donor and acceptor levels. We consider that this behavior can allow the purposeful design of the insulation property in MLCC. Thus our characterization technique using the combination of optical reflectance spectroscopy and PYS is important for the improvement of MLCC capability.

3.2 Bent band structure induced by electric polarization

We checked spectra with angle-integrated HAXPES in survey setting (TOA = 88.3°) and then confirmed peak selection, with the result that Ti-2$p_{3/2}$, O-1s, Ba-3$d_{5/2}$, and valence band in BTO as seen in Fig. 3.4, and O-1s in ALO were selected. Then, we changed angular-resolved setting (TOA = 35°) and analyzed the observed atomic orbitals with the following process: (1) background was subtracted by Shirley method; (2) subtracted spectrum was fitted by Voigt function (see gray curves in the inset of Fig. 2.5); (3) the binding energy of the atomic orbital was estimated to be the center position of FWHM. Finally, the depth-dependence of the energy shift in the atomic orbital was determined. Emission angles of 5o to 65° correspond to photoelectron emissions from the surface to a deeper region, respectively. As shown in spectra of ALO sample (inset of Fig. 2.5), O-1s splits into two peaks: one in the vicinity of 532.5 eV and another in the vicinity of 530.6 eV. With increasing sample depth, the magnitude of the lower-energy peak increases gradually. So the higher- and the lower-energy peaks are assigned to ALO and NSTO, respectively. Electronic states of each atomic configuration in heterostructure can be thus observed with depth-resolved photoemission signal.

No extrinsic charging effect was observed in our experimental data. Such a charge is often seen in photoemission experiments, where it degrades the accuracy of the data. In an extrinsic charge situation, the energy level of photoelectrons at the surface is often altered by the electric field of the surface space charge, expanding the distribution of kinetic energy and resulting in a spectral profile that increases in width as the depth decreases towards the surface. However, we confirmed that the Gaussian width of the Voigt function was

almost constant with respect to the emission angle, i.e. the distribution of kinetic energy was not expanded. Thus we conclude that there was no surface charge on our samples in the present study. Electron beam irradiation by the flood gun was not used, to avoid spectral distortion. Also, the effect of surface photovoltage can be escaped because the photon flux of 2.3×10^{16} photons/(cm^2 s) [38] is enough low.

Figure 3.5 shows AR-HAXPES spectra of Ti-2$p_{3/2}$ in 5 nm thick BTO observed at various depths. The peak shifts to a higher binding energy region with increasing escape depth. Valence band shows similar behavior to core-level binding-energy shift (Fig. 3.6). The valence band consists of three electronic states: one pure O-2p orbital and two O-2p and Ti-3d hybridized states are called as regions A, B and C, respectively [22, 41]. We firstly succeeded to observe depth profiles of the electronic structure of ferroelectrics. [44]

For a quantitative discussion of the energy shift in atomic orbitals, we fitted the changes by superposition of Voigt functions. Figures 3.7 and 3.8 shows the depth-dependence of binding energies of core levels and valence band in BTOs. In the 5 nm thick sample without top electrode as seen in Figs. 3.7(a) and 3.8, all atomic orbitals have two inflection points at emission angles of 15° and 45°. In the internal layer of BTO (corresponding to emission angles 15°–45°), the binding energy increases monotonically with increasing depth. This energy shift behavior is consistent with a potential slope where the electric polarization points into the NSTO substrate as confirmed by PFM measurement. Thus we can assign that this slope appeared in the internal layer as ferroelectric band bending (FEBB) induced by electric polarization.

It is noted that incomplete screening exists on the surface because our sample has no top electrode, suspecting that a depolarization field cancels out the formation of FEBB. We checked a thickness dependence of FEBB slope. The energy shifts of Ti-2$p_{3/2}$ core

level in BTO with a thickness of 5 and 15 nm are 0.17 and 0.11 eV, respectively (see Figs. 3.7(a) and 3.7(b)). According to Ref. [45], the electric polarization has values of 12 and 25 μC/cm^2 with 5 and 15 nm, respectively. Since an electrostatic potential V is proportional to q/r, we compared $V/(q/r)$ in the 15 nm thick BTO to that in 5 nm, resulting these values are good agreement with ~ 0.7. Here q and r are represented by bound charges and the film thickness. Thus, we concluded that the slope in the internal layer is FEBB. Strong depolarization field often induces to form the polydomain structure in thin films [32]. Although our samples possibly have polydomain structure because of no top electrode, monodomain structure was confirmed as seen in Fig. 2.4. We concluded that the potential slope induced by electric polarization has been observed as FEBB with AR-HAXPES.

At the surface (corresponding to emission angles 5°–15°), the energy shift is suppressed. This behavior implies the polarization reduction caused by surface relaxation even though the polarization in thin films is retained by an epitaxial strain. The flat surface-potential appears, is called as a surface band bending (SBB). If a top electrode is deposited on the surface of BTO, surface polarization can be sufficiently screened and stabilized, resulting that energy shift increases. We confirmed disappearance of SBB and increase of FEBB slope in Pt sputtered BTO (see red dashed line in Fig. 3.7(a)). The interface is determined by the second inflection point between emission angles of 45° and 50°. In the deeper region corresponding to emission angles 45°–65°, the slope of energy shift shows non-linearity compared with the internal layer. Lattice mismatch occurs at the interface causing a strong strain. It induces a small energy shift at the terminal of BTO. This modulated FEBB is interpreted as an interfacial band bending (IBB). Valence band shows a similar behavior of the core levels (Fig. 3.8).

When AR-HAXPES observes the whole region from the surface to the interface between BTO and NSTO as in Figs. 3.7(a) and 3.8, the energy level of all atomic orbitals has the three components of SBB, FEBB and IBB. Based on our band-bending lineup as described above, we discuss a band bending structure induced by the electric polarization i.e. FEBB. The polarization produces a gradual change of electrostatic potential in a ferroelectric crystal. Since such a potential has a slope, the binding energy increases with increasing depth in the sample, as seen in FEBB component. Electronic carriers in BTO move to the BTO/NSTO interface along the potential slope, so that a depletion region is formed in the inner layer of BTO. The polarization thus remains in BTO, forming FEBB states. In our experiment, an electronic structure bent by the electric polarization is observed as a binding energy shift of atomic orbitals. All atomic orbitals show similar behavior, but the magnitude of the energy shift derived from FEBB is different. Ti-$2p_{3/2}$, O-1s and Ba-$3d_{5/2}$ have energy shift of 0.17, 0.11 and 0.07 located at binding energy of 459.1, 530.5 and 779.6 eV, respectively (see Fig. 3.7(a)). The magnitude decreases with increasing the binding energy. This behavior can be explained by the fact that the atomic orbital with low binding energy easily changes its energy by the external field due to electric polarization. In contrast, the valence band shows a different behavior (see Fig. 3.8). Regions B and C which contain covalent Ti-3d and O-2p mixed states show larger energy shift than non-covalent region A. Energy shift of mixed states has binding energy dependence. But nearly pure oxygen states do not. Finally, we demonstrate that the band bending structure can change its slope by the switching of polarization as shown in Fig. 3.9. Our result experimentally proves ferroelectric band-bending structure, which absolutely corresponds to the theoretical prediction [12].

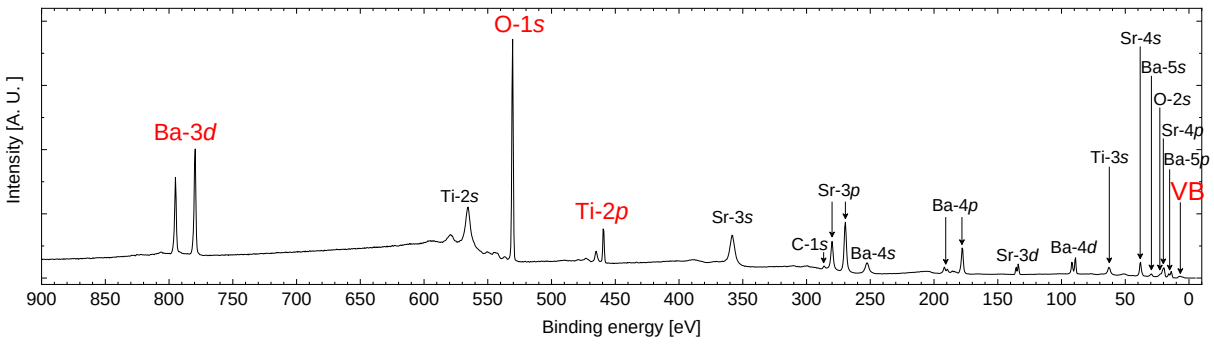

Figure 3.4: Angle-integrated HAXPES spectra of the 5 nm thick BTO.

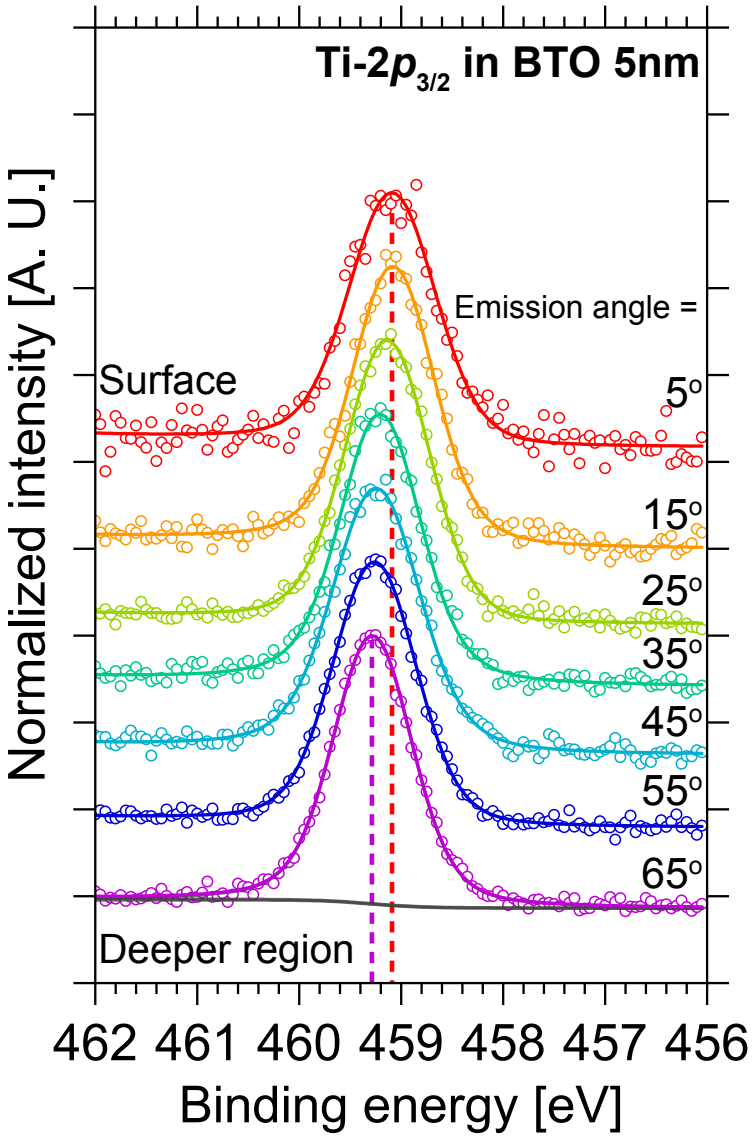

Figure 3.5: AR-HAXPES spectra of Ti-2$p_{3/2}$ in the 5 nm thick BTO observed at various depths. Red and purple circles are surface and deeper regions, respectively. In the spectrum at emission angle = 65°, curves of background and Voigt function are drawn as gray lines.

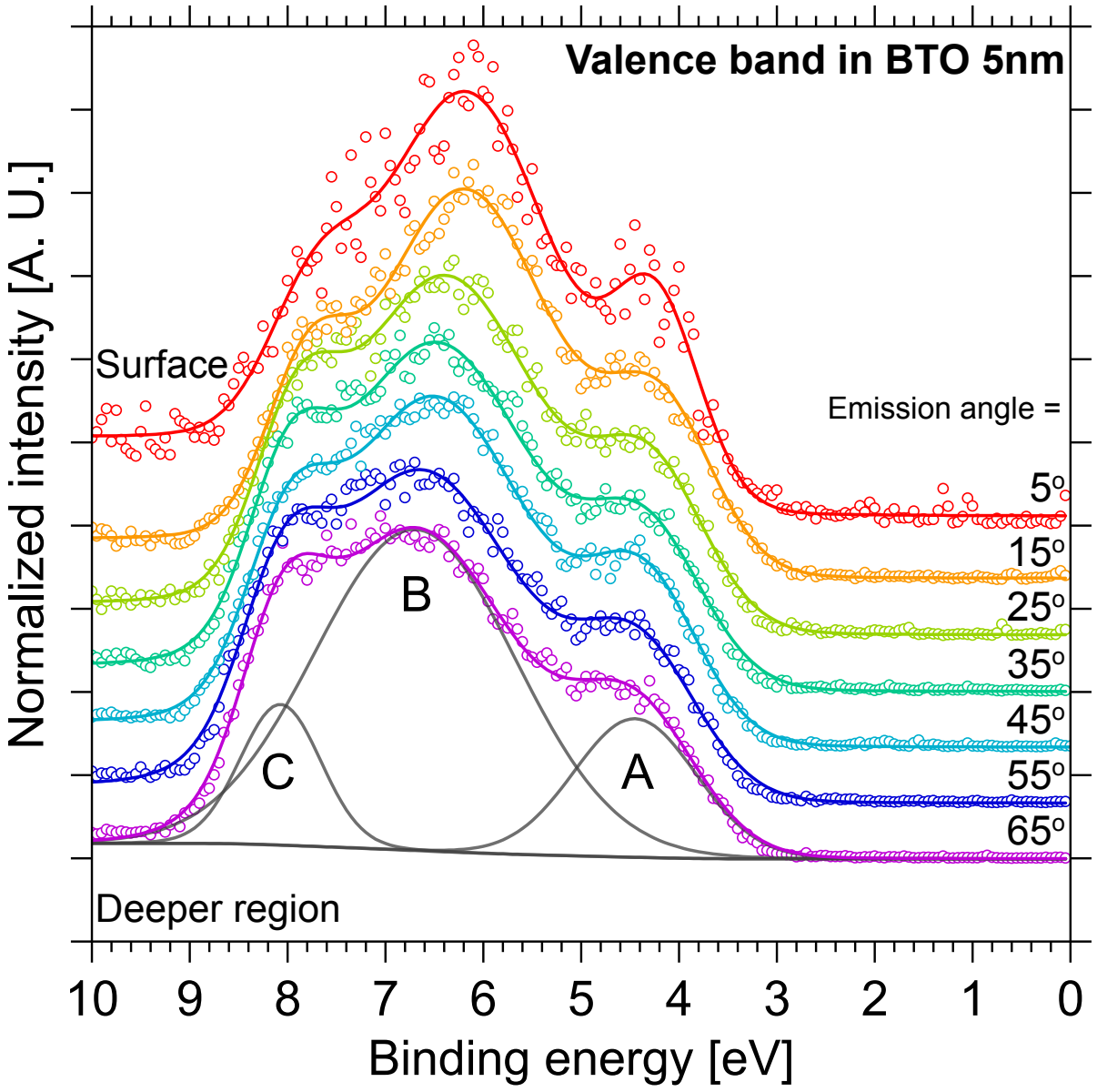

Figure 3.6: AR-HAXPES spectra of valence band in 5 nm thick BTO observed at various depths. Red and purple circles are surface and deeper regions, respectively. In the spectrum at emission angle = 65°, curves of background and Voigt function are drawn as gray lines.

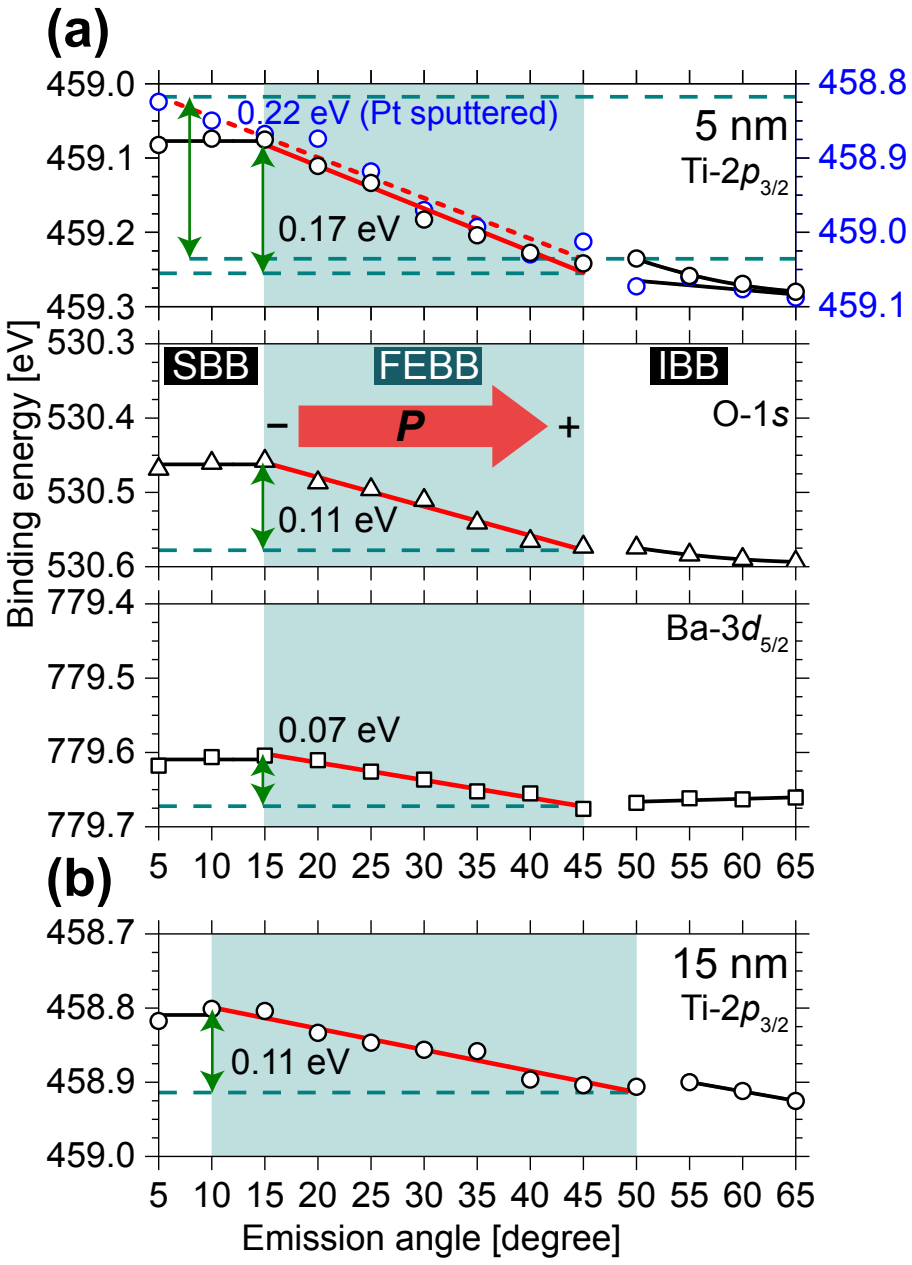

Figure 3.7: Depth dependence of binding energies of BTO: (a) Ti-$2p_{3/2}$, O-1s, Ba-$3d_{5/2}$ in 5 nm thickness and (b) Ti-$2p_{3/2}$ in 15 nm. Dots indicate the peak energy estimated by the center position of FWHM at each emission angle. Solid and dashed red lines are fitted by a linear function. Green arrows show the energy shift in FEBB. Red arrows indicate the direction of electric polarization.

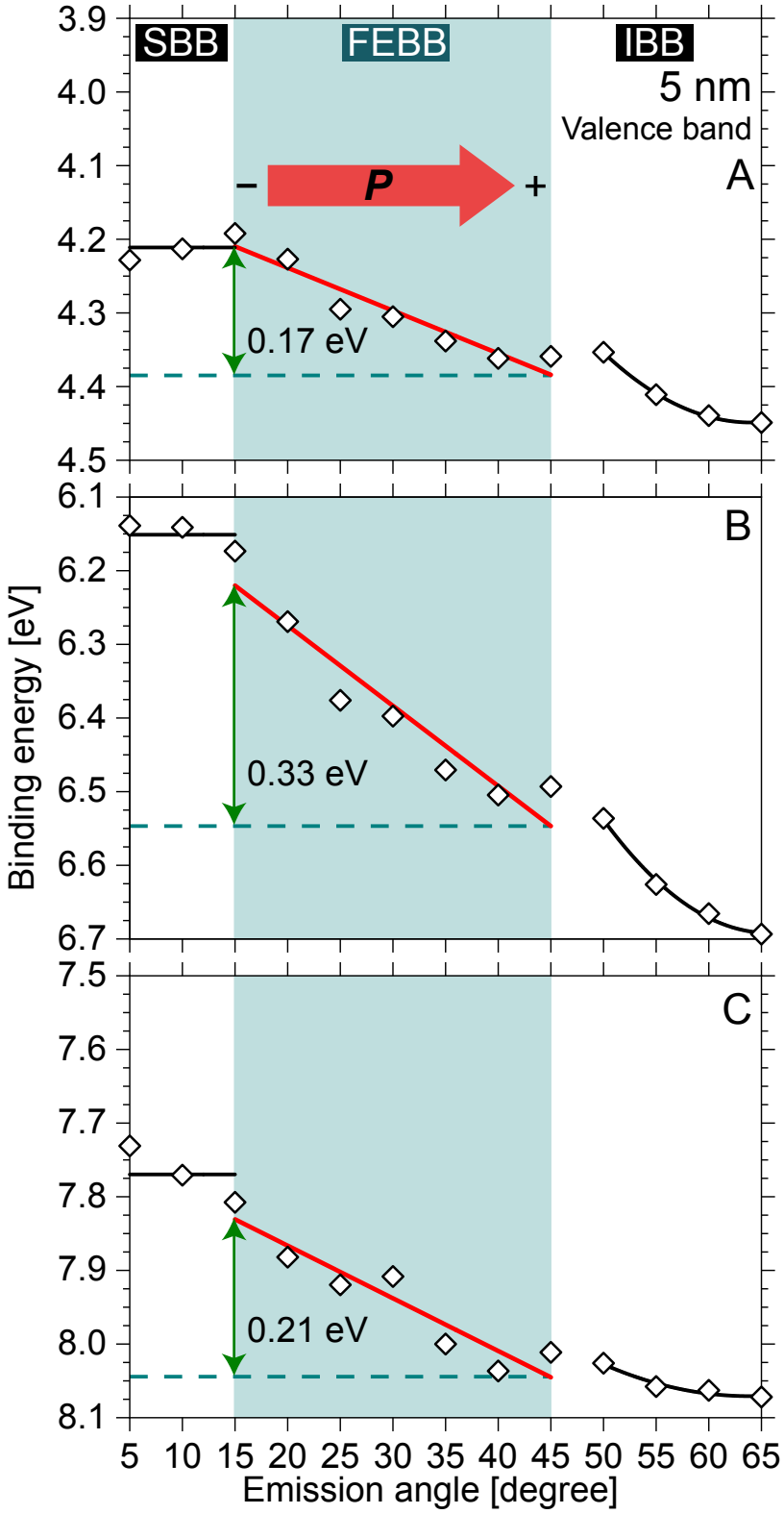

Figure 3.8: Depth dependence of binding energies of valence band in the 5 nm thick BTO. Dots indicate the peak energy estimated by the center position of FWHM at each emission angle. Solid and dashed red lines are fitted by a linear function. Green arrows show the energy shift in FEBB. Red arrows indicate the direction of electric polarization.

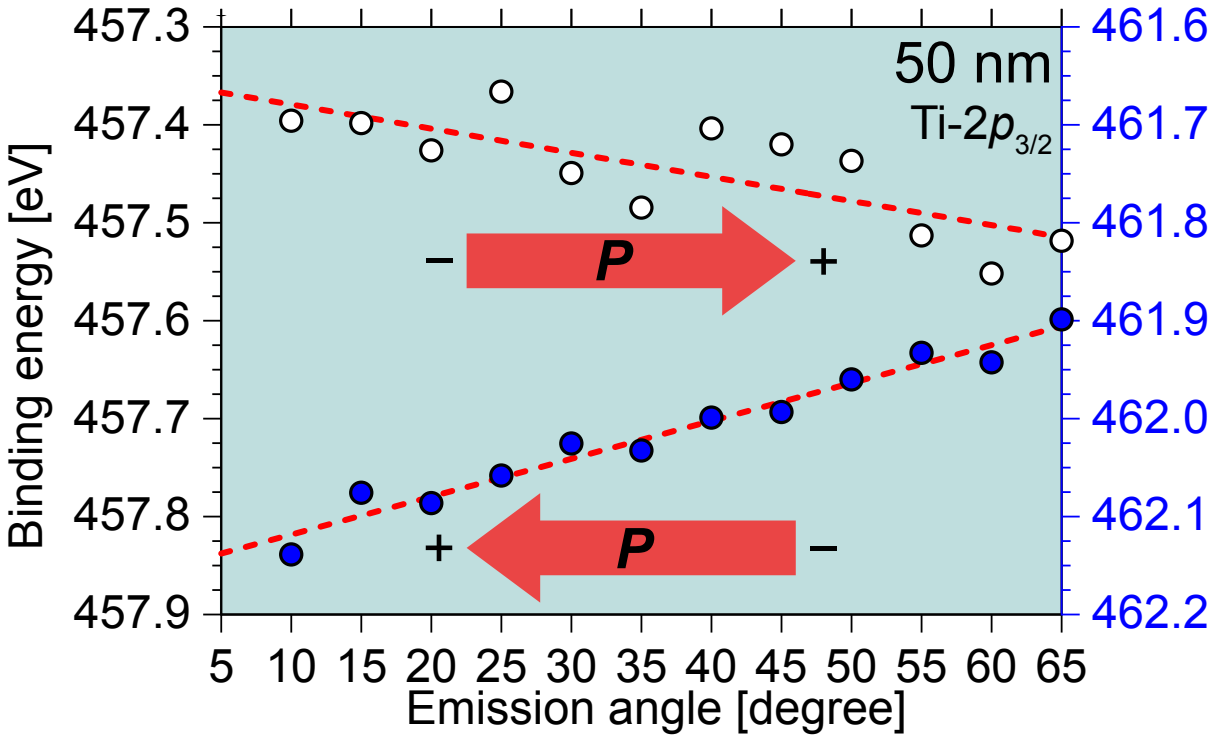

Figure 3.9: Depth dependence of binding energies of Ti-2$p_{3/2}$ in 50 nm thick BTO. Dots indicate the peak energy estimated by the center position of FWHM at each emission angle. Solid and dashed red lines are fitted by a linear function. Green arrows show the energy shift in FEBB. Red arrows indicate the direction of electric polarization.

Chapter 4

SUMMARY

We can summarize the present study as follows:

(1) In semiconducting property of ferroelectric BTO, systematic variation in the band energy levels was found that correlated with the introduction of vacancies. PYS provided direct observation of the occupancy level of electrons, which is altered by the presence of oxygen and barium vacancies. In addition, the conduction band deviation from the vacuum level was determined by optical reflectance spectroscopy. Semiconducting behavior in ferroelectrics is distinct from ion substitutions treated in covalent semiconductors such as III-IV elements.

(2) Based on above study, we proceeded in further study, the elucidation of bent structure of ferroelectrics. Ferroelectric band bending has been observed successfully in the depth profiles of atomic orbitals of AR-HAXPES spectra of ferroelectric BTO thin films. The ferroelectric bent band structure is separated into three depth regions; band structure shows a potential slope along to the electric polarization, and the surface and interface are slightly changed. In the ferroelectric bent band structure, we found that the magnitude of the energy shift depends on the binding energy and covalency states and the direction of the shift is controlled by the polarization reversal. Its means that this band bending structure can change its slope by switching polarization.

Our experimental result elucidates the existence of ferroelectric band-bending structure and its mechanism becomes clear, which guarantees further development of FeRAM and PV devices.

References

[1] J. F. Scott, Ferroelectric Memories, Vol. 3, Springer-Verlag berlin Heidelberg New York, 2000.

[2] T. Choi, S. Lee, Y. J. Choi, V. Kiryukhin, S.-W. Cheong, Switchable ferroelectric diode and photovoltaic effect in bifeo3, Science 324 (5923) (2009) 63–66.

[3] X. Liu, K. Kitamura, K. Terabe, H. Hatano, N. Ohashi, Photocatalytic nanoparticle deposition on li nb o 3 nanodomain patterns via photovoltaic effect, Appl. Phys. Lett. 91 (4) (2007) 044101.

[4] S. V. Kalinin, D. A. Bonnell, T. Alvarez, X. Lei, Z. Hu, J. H. Ferris, Q. Zhang, S. Dunn, Atomic polarization and local reactivity on ferroelectric surfaces: a new route toward complex nanostructures, Nano Lett. 2 (6) (2002) 589–593.

[5] E. Y. Tsymbal, A. Gruverman, Ferroelectric tunnel junctions: beyond the barrier, Nat. Mater. 12 (7) (2013) 602–604.

[6] V. M. Fridkin, Ferroelectric semiconductors, Consultants Bureau, 1980.

[7] R. E. Cohen, Origin of ferroelectricity in perovskite oxides, Nature 358 (6382) (1992) 136–138.

[8] Y. Kuroiwa, S. Aoyagi, A. Sawada, J. Harada, E. Nishibori, M. Takata, M. Sakata, Evidence for pb-o covalency in tetragonal pbtio 3, Physical Review Letters 87 (21) (2001) 217601.

[9] T. Kimura, T. Goto, H. Shintani, K. Ishizaka, T. Arima, Y. Tokura, Magnetic control of ferroelectric polarization, nature 426 (6962) (2003) 55–58.

[10] M. E. Lines, A. M. Glass, Principles and Applications of Ferroelectrics and Related Materials, Oxford University Press, 1977.

[11] P. Wurfel, I. Batra, Depolarization-field-induced instability in thin ferroelectric films—experiment and theory, Physical Review B 8 (11) (1973) 5126.

[12] X. Liu, J. D. Burton, E. Y. Tsymbal, Enhanced tunneling electroresistance in ferroelectric tunnel junctions due to the reversible metallization of the barrier, Phys. Rev. Lett. 116 (19) (2016) 197602.

[13] E. Y. Tsymbal, H. Kohlstedt, Tunneling across a ferroelectric, Science 313 (5784) (2006) 181–183.

[14] V. Garcia, S. Fusil, K. Bouzehouane, S. Enouz-Vedrenne, N. D. Mathur, A. Barthelemy, M. Bibes, Giant tunnel electroresistance for non-destructive readout of ferroelectric states, Nature 460 (7251) (2009) 81–84.

[15] Z. Wen, C. Li, D. Wu, A. Li, N. Ming, Ferroelectric-field-effect-enhanced electroresistance in metal/ferroelectric/semiconductor tunnel junctions, Nat. Mater. 12 (7) (2013) 617–621.

[16] Z. Xi, J. Ruan, C. Li, C. Zheng, Z. Wen, J. Dai, A. Li, D. Wu, Giant tunnelling electroresistance in metal/ferroelectric/semiconductor tunnel junctions by engineering the schottky barrier, Nature communications 8 (2017) 15217.

[17] H. Matsuo, Y. Kitanaka, R. Inoue, Y. Noguchi, M. Miyayama, Cooperative effect of oxygen-vacancy-rich layer and ferroelectric polarization on photovoltaic properties in bifeo3 thin film capacitors, Appl. Phys. Lett. 108 (3) (2016) 032901.

[18] H. Ibach, H. Lüth, Solid-state physics: an introduction to principles of material science, Advanced Texts in Physics, Springer-Verlag berlin Heidelberg New York, 2003.

[19] N. Shibata, S. D. Findlay, H. Sasaki, T. Matsumoto, H. Sawada, Y. Kohno, S. Otomo, R. Minato, Y. Ikuhara, Imaging of built-in electric field at a pn junction by scanning transmission electron microscopy, Sci. Rep. 5 (2015) 10040.

[20] M. Holma, M. Kitamura, H. Chen, Electronic structure of barium titanate studies by the extended hückel tight-binding method, Journal of applied physics 76 (1) (1994) 451–454.

[21] R. E. Cohen, Periodic slab lapw computations for ferroelectric batio 3, Journal of Physics and Chemistry of Solids 57 (10) (1996) 1393–1396.

[22] L. T. Hudson, R. L. Kurtz, S. W. Robey, D. Temple, R. L. Stockbauer, Photoelectron spectroscopic study of the valence and core-level electronic structure of batio 3, Physical Review B 47 (3) (1993) 1174.

[23] L. T. Hudson, R. L. Kurtz, S. W. Robey, D. Temple, R. L. Stockbauer, Surface core-level shifts of barium observed in photoemission of vacuum-fractured batio 3 (100), Physical Review B 47 (16) (1993) 10832.

[24] D. M. Smyth, The defect chemistry of metal oxides, Oxford University Press (2000) 304.

[25] H. Ihrig, D. Hennings, Electrical transport properties of n-type bati o 3, Physical Review B 17 (12) (1978) 4593.

[26] T. Kolodiazhnyi, Insulator-metal transition and anomalous sign reversal of the dominant charge carriers in perovskite batio 3- δ, Physical Review B 78 (4) (2008) 045107.

[27] X. Guo, C. Pithan, C. Ohly, C.-L. Jia, J. Dornseiffer, F.-H. Haegel, R. Waser, Enhancement of p-type conductivity in nanocrystalline ba ti o 3 ceramics, Applied Physics Letters 86 (8) (2005) 082110.

[28] R. Scharfschwerdt, A. Mazur, O. F. Schirmer, H. Hesse, S. Mendricks, Oxygen vacancies in bati o 3, Physical Review B 54 (21) (1996) 15284.

[29] S. Lee, C. A. Randall, Z.-K. Liu, Modified phase diagram for the barium oxide–titanium dioxide system for the ferroelectric barium titanate, Journal of the American Ceramic Society 90 (8) (2007) 2589–2594.

[30] F. Izumi, K. Momma, Three-dimensional visualization in powder diffraction, in: Solid State Phenomena, Vol. 130, Trans Tech Publ, 2007, pp. 15–20.

[31] K. J. Choi, M. Biegalski, Y. L. Li, A. Sharan, J. Schubert, R. Uecker, P. Reiche, Y. B. Chen, X. Q. Pan, V. Gopalan, et al., Enhancement of ferroelectricity in strained batio3 thin films, Science 306 (5698) (2004) 1005–1009.

[32] C. Lichtensteiger, S. Fernandez-Pena, C. Weymann, P. Zubko, J.-M. Triscone, Tuning of the depolarization field and nanodomain structure in ferroelectric thin films, Nano letters 14 (8) (2014) 4205–4211.

[33] Y. Nakayama, S. Machida, T. Minari, K. Tsukagishi, Y. Noguchi, H. Ishii, Direct observation of the electronic states of single crystalline rubrene under ambient con-

dition by photoelectron yield spectroscopy, Applied Physics Letters 93 (17) (2008) 397.

[34] M. Uda, Open counter for low energy electron detection, Japanese Journal of Applied Physics 24 (S4) (1985) 284.

[35] E. O. Kane, Theory of photoelectric emission from semiconductors, Physical review 127 (1) (1962) 131.

[36] T. Toyoda, W. Yindeesuk, T. Okuno, M. Akimoto, K. Kamiyama, S. Hayase, Q. Shen, Electronic structures of two types of tio 2 electrodes: inverse opal and nanoparticulate cases, RSC Advances 5 (61) (2015) 49623–49632.

[37] J. Szuber, New procedure for determination of the interface fermi level position for atomic hydrogen cleaned gaas (100) surface using photoemission, Vacuum 57 (2) (2000) 209–217.

[38] E. Ikenaga, M. Kobata, H. Matsuda, T. Sugiyama, H. Daimon, K. Kobayashi, Development of high lateral and wide angle resolved hard x-ray photoemission spectroscopy at bl47xu in spring-8, J. Electron Spectrosc. Relat. Phenom. 190 (2013) 180–187.

[39] J. J. Yeh, I. Lindau, Atomic subshell photoionization cross sections and asymmetry parameters: 1 z 103, At. Data Nucl. Data Tables 32 (1) (1985) 1–155.

[40] R. Federicci, S. Holé, A. F. Popa, L. Brohan, B. Baptiste, S. Mercone, B. Leridon, Rb 2 ti 2 o 5: Superionic conductor with colossal dielectric constant, Physical Review Materials 1 (3) (2017) 032001.

[41] P. Pertosa, F. M. Michel-Calendini, X-ray photoelectron spectra, theoretical band structures, and densities of states for bati o 3 and knb o 3, Physical Review B 17 (4) (1978) 2011.

[42] Unpublished.

[43] N. Oshime, J. Kano, N. Ikeda, T. Teranishi, T. Fujii, T. Ueda, T. Ohkubo, Quantitative study of band structure in batio3 particles with vacant ionic sites, Journal of Applied Physics 120 (15) (2016) 154101.

[44] N. Oshime, J. Kano, E. Ikenaga, S. Yasui, Y. Hamasaki, S. Yasuhara, S. Hinokuma, N. Ikeda, P.-E. Janolin, J.-M. Kiat, M. Itoh, T. Yokoya, T. Fujii, A. Yasui, H. Osawa, Bent electronic band structure induced by electric polarization in ferroelectric batio3, submitted.

[45] Y. Kim, D. Kim, J. Kim, Y. Chang, T. Noh, J. Kong, K. Char, Y. Park, S. Bu, J.-G. Yoon, et al., Critical thickness of ultrathin ferroelectric ba ti o 3 films, Applied Physics Letters 86 (10) (2005) 102907.